Nanocluster superstructures assembled via surface ligand switching at high-temperature

Grayson Johnson[1,†], Moon Young Yang[2,†], Chang Liu[1,†], Hua Zhou[3], Xiaobing Zuo[3], Diane A. Dickie[1], Sihan Wang[4], Wenpei Gao[4], Bukuru Anaclet[1], Frédéric A. Perras[5], Fuyan Ma[6], Chenjie Zeng[6], Da Wang[7], Sara Bals[7], Sheng Dai[8], Zhen Xu[9], Guoliang Liu[9], William A. Goddard III[2, *], Sen Zhang[1, *]

[1] Department of Chemistry, University of Virginia; Charlottesville, Virginia, USA;

[2] Materials and Process Simulation Center, California Institute of Technology; Pasadena, California, USA;

[3] X-ray Science Division, Advanced Photon Source, Argonne National Laboratory; Lemont, Illinois, USA;

[4] Department of Materials Science and Engineering, North Carolina State University; Raleigh, North Carolina, USA;

[5] Ames National Laboratory, Iowa State University; Ames, Iowa, USA;

[6] Department of Chemistry, University of Florida; Gainesville, Florida, USA;

[7] EMAT and NANOlab Center of Excellence, University of Antwerp; Groenenborgerlaan 171, Antwerp, Belgium;

[8] Chemical Sciences Division, Oak Ridge National Laboratory; Oak Ridge, Tennessee, USA.

[9] Department of Chemistry, Virginia Tech, Blacksburg, Virginia, USA.

†These authors contributed equally.

*Corresponding Authors:

Email for W.A.G.: wag@caltech.edu; ORCID:0000-0003-0097-5716

Email for S.Z.: sz3t@virginia.edu; ORCID: 0000-0002-1716-3741

Abstract: Superstructures with nanoscale building blocks, when coupled with the precise control of the constituent units, open opportunities in rationally designing and manufacturing desired functional materials. Yet, synthetic strategies for the large-scale production of superstructures are scarce. We report a scalable and generalized approach to synthesizing superstructures assembled from atomically precise $Ce_{24}O_{28}(OH)_8$ and other rare earth metal oxide nanoclusters alongside a detailed description of the self-assembly mechanism. Combining operando small angle X-ray scattering, ex-situ molecular and structural characterizations, and molecular dynamics simulations indicates that a high-temperature ligand switching mechanism, from oleate to benzoate, governs the formation of the nanocluster assembly. The chemical tuning of surface ligands controls superstructure disassembly and reassembly, and furthermore, enables the synthesis of multi-component superstructures. This synthetic approach, and the accurate mechanistic understanding, are promising for the preparation of superstructures for use in electronics, plasmonics, magnetics and catalysis.

Introduction

The assembly of nanoparticles into superstructures (also called superlattices) is a promising route towards the synthesis of novel materials with properties from the collective interactions of the assembled components[1,2]. Such cross-scale orderings, coupled with the precise control of each constituent nanoparticle's physical dimensions and chemical composition, hold promise for emergent opportunities in electronics[3-6], plasmonics[7-10], magnetics[11-14], and catalysis[15-19]. Typically, the synthesis of nanoparticle superstructures relies on a dedicated control of interparticle attraction/repulsion (for example, van der Waals forces, electrostatic forces, hydrogen bonding, solvent interactions, and steric forces) to minimize disordered aggregates[20], which can be achieved by the incorporation of surface directing domains[21,22], such as in DNA- or polymer-guided assembly[7,23-25], through solvent depletion interactions[26], or through slow solvent evaporation processes[27-30]. Despite substantial progress, established superstructure synthetic methods remain low in yield and scalability. More importantly, assembly mechanisms are generally unknown, limiting our ability to rationally design superstructures. This is, in large part, due to the inaccurately defined building blocks (i.e. uniform in nanoscale size but lack atomic level precision) and the associated complexity of interparticle interactions.

Here, we report a large-scale, one-pot colloidal synthesis of superstructures comprised of atomically precise $Ce_{24}O_{28}(OH)_8$ (Ceria) and other rare earth metal nanoclusters, which informs an unprecedentedly detailed description of the self-assembly mechanism through a high-temperature ligand switching surface chemistry. Using *operando* small angle X-ray scattering (SAXS), a powerful technique capable of providing information about both superstructure ordering [31] and nanoparticle structure[32], in combination with *ex-situ* solid state nuclear magnetic resonance (SSNMR) and single crystal X-ray diffraction (SCXRD), we fully mapped the

nanocluster nucleation and assembly pathways. As illustrated in **Fig. 1**, we identified a temperature (T)-dependent surface ligand switching phenomenon, from oleate (OA) to benzoate (BA), over $Ce_{24}O_{28}(OH)_8$ building blocks that leads to formation of superstructures. Molecular dynamics (MD) simulations validated the favourable energetics of ligand switching at high temperature and the pivotal role that BA π-stacking interactions play in governing the superstructure generation. This strategy is applicable to a broad range of rare earth metal oxide nanocluster superstructures and enables the control of superstructure disassembly/reassembly through surface ligand chemistry. By utilizing different nanocluster building units, we have created multi-component superstructures and even high-entropy alloy analogous superstructures (HEAAS).

Results and Discussion

Ceria nanocluster superstructure synthesis and *operando* SAXS

Ceria superstructures were generated through a colloidal synthesis from cerium acetate refluxing in a benzyl ether solvent (20 mL) with a small amount of oleic acid for 4 hours at 290 °C. The product is a gray solid precipitate (**Supplementary Figure 1a, b**) and remains structurally stable in hexanes and isopropanol solvents. They can be readily generated on a gram scale (~4.3 g) in a single, scaled reaction using 400 mL of solvent (**Supplementary Figure 1c**). **Fig. 2a-c** and **Supplementary Figure 2** show the representative high-angle annular dark-field scanning transmission electron microscopy (HAADF-STEM) images of the as-synthesized ceria superstructures. Rod-like structures are observed on the order of 1–4 μm long and 30–100 nm across. These structures are comprised of a superlattice of monodisperse 1.4 ± 0.3 nm ceria nanoclusters.

Operando SAXS measurements were performed (**Fig. 2d-e**) to access details of the superstructure and its formation pathway. These experiments were conducted using synchrotron

hard X-rays and a specialized reactor (**Supplementary Figure 3a, b**) similar to that used in a previous study[31]. SAXS profile monitoring at T = 135 – 290 °C along the reaction show evolution of a shoulder peak at q = 0.2 $Å^{-1}$ emerging at 260 °C (**Fig. 2d**). This feature becomes more pronounced at 290 °C and fits well with a hard sphere model having a radius of 0.89 nm (**Supplementary Figure 3c**). Therefore, nanoclusters are formed in the initial stages of the reaction without the structure peaks associated with superstructures being observed. Allowing further reaction, a series of time (t)-dependent SAXS profiles is presented in **Fig. 2e** with the t = 0 min measurement occurring upon the reaction temperature reaching 290 °C. Long-range structure peaks (**Fig. 2e** and **Supplementary Figure 3d**) start to appear at 25 min and increase in intensity as the reaction progresses. These are accompanied by a large rise in the low q region associated with the scattering from the superstructures. The structure peaks are assigned to a body-centered tetragonal (*bct*) assembly (lattice parameters: a = 1.9 nm and b = c = 3.3 nm) with peak indices labeled in **Fig. 2e**. Some peaks are unobservable above the background (such as (022) or (121)) due to the 1D shape of the superstructure. Clearly, the superstructures form only at 290 °C, independently from the nanocluster generation which occurs at lower temperatures.

OA-to-BA ligand switching for superstructure formation

We found that benzyl ether solvent is critical to the formation of these assemblies. Attempting this synthesis in alternate solvents such as 1-octadecene, dioctyl ether, or diphenyl ether does not generate superstructures. Previously, the decomposition of benzyl ether into benzaldehyde and BA has been implicated in the shape variations of magnetite (Fe_3O_4) nanocrystals[33]. ^{1}H NMR analyses of benzyl ether heated to 290 °C show that this system also experiences a steady increase of benzaldehyde over time (**Supplementary Figure 4a, b**). Moreover, injecting neat, excess benzaldehyde (0.75 mL) to the synthesis at 290 °C reduces the reaction time by a factor of 4 to

yield the same superstructures. Benzaldehyde has previously been suggested as a source of BA ligands catalyzed by reaction with benzyl alcohol on yttrium oxides to yield lamellar assemblies[34]. Other metal oxides can also catalyze the Cannizzaro reaction to convert benzaldehyde to BA and benzyl alcohol[35]. We envision that, through similar means (**Supplementary Figure 5a, b**), BA is likely to form on and strongly bind to ceria nanoclusters to induce the formation of superstructures.

$^{13}C\{^{1}H\}$ cross polarization magic angle spinning (CPMAS) SSNMR was used to reveal the surface ligands of nanoclusters and superstructures. The samples collected from different reaction stages were purified and dried in vacuum prior to analysis. As displayed in **Fig. 2f**, nanoclusters isolated before superstructure formation (290 °C, t = 0 min) exhibited two major resonances around 130 ppm, typical of sp^2 hybridized C, and 40 ppm from sp^3 hybridized C. When measurement is taken for the superstructure solid, the peak near 40 ppm is significantly diminished. The sp^3 contribution is assigned to OA ligands and is thought to be completely replaced by BA in the superstructure. The broad linewidths of the resonances are assigned to the presence of paramagnetic Ce^{3+} centers (Ce^{3+} is discussed below)[36]. When $^{13}C_1$-labeled OA is used in the synthesis, OA remained undetectable in the superstructure solid, further confirming the extent of replacement. Raman spectroscopy performed on the dried superstructure confirms the presence of BA as surface ligands (**Supplementary Figure 5c and Supplementary Table 1**)[37]. Characterization of the superstructure dispersion in solution phase by ^{1}H NMR (**Supplementary Figure 6a**) provides further evidence of BA with resonances at 8.15 ppm, 7.68 ppm, and 7.52 ppm. Benzaldehyde, on the other hand, is not observed in the superstructure as is evident from the absence of a resonance at 7.88 ppm (**Supplementary Figure 6b**).

The superstructure can be dissolved to disperse the nanoclusters in non-polar solvents (such as hexanes) at room temperature by adding excess oleic acid, yielding a golden-brown dispersion

(**Supplementary Figure 7a, b**) that has a reduced absorbance of visible light compared to the assembled structures in UV-Vis analysis (**Supplementary Figure 8**). Correspondingly, disassembled nanoclusters can be seen in transmission electron microscopy (TEM) images (**Supplementary Figure 7b**) and are associated with the return of the OA sp^3 C signal in the ^{13}C SSNMR spectra (**Fig. 2f**). As such, surface BA ligands can be reversibly exchanged with OA to disassemble the superstructure. Disassembly can also be achieved using more polar solvents in the absence of OA, including pyridine, dichloromethane, and dimethylformamide (DMF), which are able to better solvate the BA-capped particles.

Surprisingly, using a pyridine ceria nanocluster solution disassembled from superstructures, we were able to obtain single crystals of the nanoclusters following the addition of acetonitrile and water. It is worth mentioning that the amount of acetonitrile needs to be carefully controlled to permit a slow crystal nucleation and growth over the course of several weeks; an excess of acetonitrile results in disordered aggregates. SCXRD results show a monoclinic $P2_1/n$ structure (**Fig. 2g** and **Supplementary Figure 9**) (lattice parameters: a = 2.13 nm, b = 2.51 nm, c = 2.55 nm, and $\beta = 92.02°$) is obtained with $Ce_{24}O_{28}(OH)_8$ nanocluster building blocks, similar to the one previously reported[38,39]. The size of the $Ce_{24}O_{28}(OH)_8$ is 1.53 nm x 1.46 nm x 1.21 nm. This matches well with the clusters observed in the TEM images (**Fig. 2a-c**). In addition, the parameters of the single crystal also resemble the body-centered tetragonal superlattice determined by SAXS, indicating a similar packing strategy in the single crystals as well as the superstructures. As illustrated in **Fig. 2g** and **Supplementary Figure 11**, each $Ce_{24}O_{28}(OH)_8$ nanocluster contains 2 Ce^{3+} and is ligated by 30 BA and 8 pyridines. These pyridines consist of 4 OH-bound (via H-bonding) and 4 Ce-bound species (**Supplementary Figure 10**). Given that the pyridine is only introduced to disassemble the superstructure for single crystal growth, the SCXRD result allows

us to further confirm that the building units in the superstructures are indeed atomically precise $Ce_{24}O_{28}(OH)_8$ units with the sole packing ligand of 30 BAs.

Matrix-assisted laser desorption/ionization-time of flight mass spectrometry (MALDI-TOF MS) was also used to characterize the disassembled ceria nanoclusters. Disassembling the superstructures in DMF and combining with an anthracene matrix, the MALDI-TOF MS spectrum in **Supplementary Figure 11** was collected. The first major spectral peak appears at 4061 m/z, which can be best assigned to $Ce_{24}O_{28}(OH)_8(BA)_1$ (theoretical m/z is 4068), and these peaks primarily repeat at the interval of 121 m/z. The difference of 121 m/z corresponds to different BA coverages. These peaks are further subdivided by units of 16 m/z, corresponding to changes in the number of O atoms in the cluster, and have varying intensities that lead to the 105 m/z separations in some of the peak maxima. The peaks terminate before the calculated maximum mass of 7580 m/z for $Ce_{24}O_{28}(OH)_8(BA)_{30}$. Clearly, the cluster is disintegrated by the laser in MALDI-TOF MS measurement (which is common for ionic clusters in MALDI-TOF MS measurement), but the result provides atomically precise characteristics of nanoclusters with BA ligands.

Succinctly summarized, OA-capped nanoclusters are first formed at 260 °C in the colloidal synthesis, and subsequently react with benzaldehyde to induce a full ligand-switching to BA at 290 °C. The high temperature reaction is required to provide benzaldehyde species through the thermal decomposition of benzyl ether solvent. The resultant BA-packed $Ce_{24}O_{28}(OH)_8$ nanoclusters serve as building blocks to construct the superstructure solids.

MD simulations

We carried out MD simulations to understand the cross-cluster interactions that drive the superstructure formation. Two models, OA-packed and BA-packed nanoclusters, were constructed

to mimic the reaction condition (**Fig. 3a, b**). Based on experimental observations, each model contains 2 $Ce_{24}O_{28}(OH)_8$ nanocluster building blocks with 60 BAs, 60 OAs, and 120 benzyl ethers, where the BAs in the OA-packed model and the OAs in the BA-packed model were protonated (labeled as pBA and pOA) to prevent their binding to nanoclusters and to retain neutrality of the system in the ligand switching. Interestingly, the BA-capped clusters spontaneously aggregate independent of their initial spacing, with the final distance between two nanoclusters becoming close to that of the single crystal structure, ~2.1 nm (**Fig. 3c**). In comparison, the cluster-cluster distance is > 3 nm for the OA-packed one, corresponding to the dispersed form in the nanocluster solution. Moreover, the BA-packed system is energetically more favorable than the OA counterpart by over 100 kcal mol^{-1} (**Fig. 3d**), which agrees with the observed OA-to-BA switching in the experiment. This energy difference is attributed mainly to improvements in the van der Waals or hydrophobic interactions (**Supplementary Figure 12 a,b**), probably dominated by π-π interactions between adjacent BAs. The BA aromatic ring on the nanocluster surface can form edge-to-face or offset stacked π-π interactions depending on the position (**Fig. 3 e,f**), providing the additional energy gain that drives the self-assembly.

The *operando* SAXS result presents slightly different cell parameters (a = 1.9 nm and $b = c$ = 3.3 nm) for the superstructure in solution phase, compared to those of the single crystal derived from SCXRD (a = 2.13 nm, b = 2.51 nm, c = 2.55 nm, and β = 92.02°). Although both structures are similar, the cell volume of the superstructure (20.7 nm^3) is larger than single crystal (13.6 nm^3). The single crystal unit cell volume can be computationally matched upon the addition of 34 BAs on each nanocluster, simulating 30 BAs and the 8 Ce-bound pyridines deciphered from SCXRD (**Fig. 4a**). The larger volume of the superstructure unit cell requires an even greater number (> 42) of bound BA, which is impossible for small nanoclusters with limited surface area. Such a

deviation is likely caused by the incorporation of non-binding benzyl ether in the superstructure in the solution phase. To confirm this, we calculated the cell volume as a function of the number of benzyl ethers incorporated (**Fig. 4b**), where the systems were considered to contain 60 BAs (30 BAs per nanocluster). Our computation demonstrates that the cell volume matches well to the experimental result, ~20.7 nm^3, when 16 benzyl ethers were included (**Fig. 4c**).

Thermogravimetric (TGA) analysis (**Supplementary Figure 13**) was used to measure the organic components of the ceria assemblies and verify that extra benzyl ether is included. It is assumed that the initial structures contain $Ce_{24}O_{28}(OH)_8$ clusters with 30 BA ligands according to SCXRD result and to maintain cluster charge neutrality and that, in the high O_2, high temperature TGA experiment, the final structures are fully oxidized to $Ce_{24}O_{48}$. It is also assumed that the first 5.1% of weight loss is from residual solvent. Based on the unaccounted mass, we calculate that 7.8 benzyl ethers per cluster are required to make up the balance, which aligns well with MD simulation. These results suggest that the self-assembled ceria superstructure in the solution phase contains 30 BAs and ~8 benzyl ethers per nanocluster in the unit cell (**Fig. 4c**).

The ceria nanocluster has (100) and (111) facets (**Fig. 4d**). O anions bonded to the central Ce of the hexagonal (111) facet repels BA, leaving an open facet. This facet, in the single crystal, binds the 4 Ce-bound pyridine ligands. The lack of pyridine in the superstructure, plus the presence of benzyl ether, leads to an altered unit cell relative to the single crystal. Furthermore, our MD simulations show that benzyl ether molecules surround the BA-packed nanoclusters across the *yz* plane (**Fig. 4c**), filling the space between the nanoclusters, while the nanoclusters connect periodically along the *x* axis with no incorporation of benzyl ether. It is along the *x* direction where the (111) facets face one another at an offset, allowing compact packing where one BA bound to

the edge of the (111) facet into fits the space above the center of the hexagon in the next cell (**Fig. 4e**), while the BAs of the edges contribute to the π-π interactions that stabilize the structure.

General synthesis of mono- and multi-element superstructures

This superstructure synthesis can be extended to many other rare earth metal oxides, including La, Sm, Eu, Gd, Tb, Ho, Er, Tm, and Yb (**Fig. 5 a-h**). Generally, their nanoclusters and superstructures resemble the ceria system with slight variations in superstructure macro-shape. These structures are also slower to form assemblies. Using LaO_x as an example for the non-Ce lanthanides, *operando* SAXS (**Fig. 5i**) showed that ordering is not observed until 110 minutes into the reaction. As with ceria, a rise in the low q region (< 0.05 $Å^{-1}$) is observed with the onset of a structure peak (q = 0.407 $Å^{-1}$). For LaO_x, this peak shows a 10 times greater full width at half maximum, and only one peak is evident, showing that this structure has more variability than the ceria. Since the ordering in the TEM images appears similar, this may be consistent with another *bct* type structure with parameters of 1.8 nm x 3.0 nm x 3.0 nm, but further corroborating evidence is required to confirm this structure. Another difference from the ceria superstructures is that these superstructures range from light brown to bright white rather than grey (**Supplementary Figure 14**). Like ceria, they can be disassembled in different solvents or via the addition of excess OA, and they have a reduced interaction with visible light (UV-Vis spectra of SmO_x and LaO_x are shown in **Supplementary Figure 15**). Unlike ceria with a dominant Ce +4 oxidation state, these other elements exist primarily in their +3 oxidation state as indicated by X-ray photoelectron spectroscopy (XPS) (**Supplementary Figure 16**), which is typical for non-Ce rare earth metal oxides.

An interesting feature of these superstructures is that the OA-capped disassembled nanoclusters can be purified and reacted in benzyl ether at 290 °C again to regenerate superstructures (**Supplementary Figure 17a,b**). The ability to disassemble and reassemble nanoclusters offers the opportunity to synthesize multi-component superstructures. As a proof-of-the-concept example, the CeO_x, LaO_x, and SmO_x superstructures were disassembled, and their nanocluster mixtures in benzyl ether were reacted to re-assemble. **Fig. 6a-f** display the low-magnification and high-magnification TEM images of the binary and ternary superstructures, confirming the efficacy of this strategy. Energy-dispersive X-ray spectroscopy (EDS) elemental mapping confirms the uniform distribution of Ce, La and Sm elements in the ternary superstructures (**Fig. 4g, h**). Two factors are thought to benefit the assembly of multi-component superstructures. First, the building blocks possess a similar size (~1.4 nm), regardless of their chemical composition. Second, the presence of benzyl ether in the superstructures enables local structural variations that compensate for the variations in the building block structures. Such size-determined binary assemblies were previously reported in the case of larger nanoparticles[40]; however, this is, to the best of our knowledge, the first such demonstration in the case of nanoclusters. More excitingly, we created a HEAAS using La, Eu, Sm, Yb, and Ce in this method, as shown in **Supplementary Figure 15c-e**. HEA is an emerging alloying strategy that involves 5+ elements in high concentration with high-entropy atomic disordering[41,42]. Our HEAAS presents a similar high-entropy state at a distinct length-scale, in which multiple nanoclusters serve as building blocks and are randomly distributed in superstructures.

Conclusion

Our experimental and computational studies demonstrate that a high-temperature ligand-switching mechanism governs assembly of atomically precise nanoclusters into superstructures.

The chemical insight presented here enables a generalized approach to synthesizing large-scale nanocluster superstructures for a wide range of rare earth metal oxides and their multi-component combinations. This unique synthetic capability may enable opportunities in studying how superstructure physical properties originate from well-defined building units or multi-component synergies in ordered structures.

Materials and Methods

Chemicals. Cerium acetate hydrate ($Ce(Ac)_3 \cdot xH_2O$, 99.9%) and lanthanum acetate hydrate ($La(Ac)_3 \cdot xH_2O$, 99.9%) were purchased from STREM Chemicals Inc. Ytterbium acetate tetrahydrate ($Yb(Ac)_3 \cdot 3H_2O$, 99.9 %) was purchased from Accela. Europium acetate hydrate ($Eu(Ac)_3 \cdot xH_2O$, 99.9%), holmium acetate hydrate ($Ho(Ac)_3 \cdot xH_2O$, 99.9%), thulium acetate hydrate ($Tm(Ac)_3 \cdot xH_2O$, 99.9%), samarium acetate hydrate ($Sm(Ac)_3 \cdot xH_2O$, 99.9%) erbium acetate tetrahydrate ($Er(Ac)_3 \cdot 4H_2O$, 99.9%), and gadolinium acetate hydrate ($Gd(Ac)_3 \cdot xH_2O$, 99.9%) were purchased from Alfa Aesar. Isopropanol (IPA, Certified ACS Plus), hexanes (Certified ACS), acetonitrile (Certified ACS), and pyridine (Certified ACS) were purchased from Fisher Chemical. Benzyl ether (99%) was purchased from Acros Chemical. Oleic acid (OAc, technical grade 90%) and benzaldehyde (Reagent Plus 99%) were purchased from Sigma Aldrich. ^{13}C labelled oleic acid (1-^{13}C, 99%) was purchased from Cambridge Isotope Laboratories, Inc. All chemicals were used without further purification.

Superstructure synthesis. Nanocluster superstructures were synthesized colloidally in a one pot synthesis of 0.5 mmol of the corresponding rare earth acetate in 20 mL of benzyl ether and 0.23 mL of OAc. The reaction mixture was heated to 150 °C for 1 hour under flowing N_2 to purge water and other impurities. Then, the reaction was heated to 290 °C, at which point the reaction mixture will reflux. The reaction was held at this temperature for at least 4 hours. The reaction mixture transforms from golden brown to a milky yellow color (Ce) or brown (other rare earth metals) when complete. After cooling to room temperature, the product was washed via centrifugation with IPA and dispersed in hexane at least twice. Washed samples manifest as a grey (Ce), white, or brown (other rare earth metals) dispersion and gently settle to the bottom. This procedure was repeated, scaling to 10 mmol of metal salt precursor without complication. The CeO_x reaction rate

was increased by introducing 0.75 mL of benzaldehyde once the reaction temperature reached 290 °C. This reaction was finished after 1 hour rather than 4 hours.

Superstructure (dis/re)assembly and multielement assembly. The purified superstructures could be disassembled by introducing 3 mL of OAc to the hexane dispersed sample. Generally, this was carried out over a few minutes. The disassembled particles were washed with acetone and redispersed in hexane. These particles could be reintroduced to 20 ml of benzyl ether and rerun through the above superstructure synthesis procedure to regenerate superstructures. By mixing nanoclusters that were disassembled and purified, binary, and ternary mixes of CeO_x, LaO_x, and SmO_x were generated. In these samples, the weights of the added metal oxides were kept equal. A quinary, HEAAS was also produced using available YbO_x, CeO_x, SmO_x, EuO_x, and LaO_x. The ratio of the precursors used for the quinary sample was approximately 1:1:1.5:2:2.

SAXS measurements. *Operando* SAXS measurements were executed in a specialized reactor as reported by Tassone *et al.*[31] (**Supplementary Figure 3a, b**). The reactions were carried out as described earlier but scaled to the 10 mL to accommodate the smaller reactor. Measurements were performed at beam 12-ID-B of the Advanced Photon Source at Argonne National Laboratory. The X-ray wavelength, λ, was set to 0.886 Å. Scattered X-ray intensities were measured with a Pilatus 2M detector (DECTRIS Ltd). The distance from sample to detector is 2 m. Each measurement is an average of 10 exposures of 0.5 s each and occurred at intervals of 60 s. 1D SAXS curves were generated by averaging the 2D images azimuthally, performing a solid angle correction, and normalizing to the unimpeded transmitted X-ray beam in the Irena software package developed at beamline 12-ID-B. The 1D SAXS curves were fit in the SasView package (http://www.sasview.org/) to a spherical model.

NMR measurements. ^{1}H NMR spectra were recorded using a Bruker AV800 spectrometer. All SSNMR experiments were performed using an Agilent DD2 400 MHz NMR spectrometer equipped with a Chemagnetics 3.2 mm MAS probe. ^{13}C MAS spectra were acquired both using cross-polarization (CP) as well as using a Bloch decay sequence. The Bloch decay experiment is expected to be better quantitative while the CP experiment accentuates the solid components of the mixture. All hard pulses used 100 kHz RF power for both the Bloch decay and CP experiments while CP was achieved using a 2 ms contact time. In all cases a total of 1024 scans were accumulated, with the recycle delay set to 2 s and 4 s for the CP and Bloch decay experiments, respectively.

MALDI-TOF MS. MALDI-TOF MS was performed on a Bruker Ultraflex III MALDI-TOF mass spectrometer. Assembled structures were disassembled in DMF (10 mg mL^{-1}) and combined with 10 mg mL^{-1} anthracene matrix in DMF in a 1:1 v/v ratio. The solution (0.8 μL) was dried on a stainless-steel MALDI target plate two times. Calibration of the instrument in the 4 – 20 kDa range was performed with a mixture of insulin, cytochrome, myoglobin, and ubiquitin.

UV-Vis Measurements. Assembled structures were dispersed in hexanes with and without oleic acid in a 1 cm path length quartz cuvette for absorbance measurements. A Shimadzu UV-2600 spectrophotometer was used for these measurements. Each sample was measured against a background of pure hexanes.

TGA Analysis. Organic component percentage was studied on a Discovery TGA5500 thermogravimetric analyzer (TA Instruments). Samples were prepared by centrifugation and air drying. The samples were heated from room temperature to 700 ºC at a ramp rate of 10 ºC min^{-1} in air to fully pyrolyze organic and volatile components.

SCXRD. The superstructures were washed with IPA and dispersed in minimal pyridine to yield a transparent, golden solution. This solution was filtered through a 0.45 μm syringe filter.1% DI water and 2 equivalents of acetonitrile were added to the solution. Crystals were formed after sitting at least 4 weeks undisturbed. Single crystals of the ceria nanoclusters were coated with Paratone oil on a MiTeGen Microloop sample holder. The X-ray intensity data were measured on Bruker D8 Venture Kappa four-circle diffractometer system equipped with an Incoatec IμS 3.0 micro-focus sealed X-ray tube (Cu Kα, λ = 1.54178 Å) and a HELIOS EF double bounce multilayer mirror monochromator. The frames were integrated with the Bruker SAINT software package using a narrow-frame algorithm. The Multi-Scan method (SADABS) was used to correct for absorption effects. Structure solutions were refined in the Bruker SHELXTL Software Package[43] within APEX and OLEX2[44]. Non-hydrogen atoms were refined anisotropically and hydrogen atoms were placed in geometrically calculated positions with U_{iso} = 1.2 U_{equiv} of the parent atom. The relative occupancy of each set of disordered atoms was freely refined. Constraints and restraints were used on the anisotropic displacement parameters and bond lengths of the disordered atoms. Additional solvent located in the crystal lattice was severely disordered and could not be adequately modeled with or without restraints. Thus, the structure factors were modified using the PLATON SQUEEZE technique, in order to produce a "solvate-free" structure factor set. PLATON reported a total electron density of 225 e^- and total solvent accessible volume of 1152 $Å^3$.

Theoretical calculations. The formation and structures of $Ce_{24}O_{28}(OH)_8$ nanocluster superstructures were studied using MD simulations. The $Ce_{24}O_{28}(OH)_8$ nanocluster was constructed based on the experimentally obtained single-crystal structure. For the atomic charge, we assigned +4e (22 atoms) and +3e (2 atoms) for Ce atoms, and -2e (36 atoms) for O atoms,

where 8 O atoms were capped by protons with +1e. Thus, one nanocluster has a total of +30e charges, which was compensated by ligands (-1e for each acid). The charges on Ce atoms were adjusted slightly when the number of ligands was less or greater than 30 to keep the system neutral. These assigned charges on the nanocluster and ligands were reduced by a factor of 0.5 to take account of the screening effect. Otherwise, the unshielded Coulombic interactions between the point charges in the nanocluster and ligands could lead to an unreasonable structure. The universal force field (UFF)[45] was used to describe the forces involving the ceria nanoclusters. For organic ligands, we used the CHARMM force field, which was generated by the CHARMM-GUI [46] and then converted into the LAMMPS format by using InterMol[47]. All MD simulations were carried out using the LAMMPS software[48] with the following steps:

1) Minimization by the steepest descent method was followed by NVT (constant number of molecules, volume, and temperature) simulation at 10 K for 10 ps to generate initial velocities.

2) Heating the system from 10 K to 563 K over 100 ps using NVT, where the cell volume calculation as a function of the number of benzoic acids (**Fig. 3i**) was performed at 300 K to match the condition of the single-crystal experiment at room temperature.

3) NPT (constant number of molecules, pressure, and temperature) production runs at the target temperature for 3 ns, where the Nose-Hoover thermostat and barostat was used with 0.1 ps and 1 ps damping times for temperature and pressure, respectively.

All initial structures were generated by packmol[49]. VMD[50] was used for the visualization and analysis of the MD trajectories.

Other characterizations. TEM images were obtained on a FEI Tecnai Spirit operated at 120 kV. Raman spectroscopy measurements were performed on a Renishaw InVia^{TM} confocal Raman

391 microscope with an Ar^+ excitation laser wavelength of 514 nm. XPS was carried out using a PHI
392 VersaProbe III equipped with a monochromatic Al K-alpha (1486.6 eV) X-ray source with
393 spherical capacitor energy analyzer to examine oxidation states of the lanthanide elements. Spectra
394 were measured with a 100 μm spot size and 55 eV pass energy. Charging corrections to the binding
395 energy were made by reference to graphitic C 1s at 284.5 eV. Data were analyzed in PHI Multipak
396 9.8.0.19 where a Shirley background was subtracted to remove inelastic scattering components
397 except in the case of Gd, where the Shirley background inappropriately cut off above the
398 background levels. HAADF-STEM images were obtained in an aberration-corrected 'cubed'
399 Thermo Fisher Scientific Themis Z 60-300 electron microscope operated at 200 kV from EMAT.
400 Thermo Scientific Titan aberration corrected STEM (200 kV) with a Super-X G1 EDS detector
401 were used for STEM-EDS measurement.

402 **Data Availability**

403 The data supporting the finding of the study are available in the paper and its Supplementary
404 Information. Source data are provided with this paper. Crystallographic data for the structure
405 reported in this Article have been deposited at the Cambridge Crystallographic Data Centre, under
406 deposition number CCDC 2157579. Copies of the data can be obtained free of charge via
407 https://www.ccdc.cam.ac.uk/structures/.

408 **Acknowledgments:** This work was supported by the US National Science Foundation (CBET-
409 2004808) and the Sloan Research Fellowship. We acknowledge UVA's Nanoscale Material
410 Characterization Facility (NMCF) for use of the XPS and SCXRD acquired under NSF MRI award
411 DMR-1626201 and CHE-20188780, respectively. G.J. acknowledges the support from the U.S.
412 Department of Energy (DOE), Office of Science, Office of Workforce Development for Teachers
413 and Scientists, Office of Science Graduate Student Research (SCGSR) program. The SCGSR

program is administered by the Oak Ridge Institute for Science and Education for the DOE under contract number DE-SC0014664. This work benefited from the use of the SasView application, originally developed under NSF Award DMR-0520547. SasView also contains code developed with funding from the EU Horizon 2020 program under the SINE2020 project Grant No 654000. This research used resources of the Advanced Photon Source, a U.S. DOE Office of Science User Facility operated for the DOE Office of Science by Argonne National Laboratory, under Contract No. DE-AC02-06CH11357. D.W. acknowledges an Individual Fellowship funded by the Marie Skłodowska-Curie Actions (MSCA) in Horizon 2020 program (Grant 894254 SuprAtom). S.B. acknowledges the support from the European Research Council (Grant No. 815128-REALNANO). The electron microscopy work was performed in part at the Analytical Instrumentation Facility (AIF) at North Carolina State University, which is supported by the State of North Carolina and the National Science Foundation (award number ECCS-2025064). The AIF is a member of the North Carolina Research Triangle Nanotechnology Network (RTNN), a site in the National Nanotechnology Coordinated Infrastructure (NNCI). G. L. gratefully acknowledges the funding support by US NSF (DMR-1752611) and the Dean's Discovery Fund at Virginia Tech. S.D. acknowledges the support from the U.S. DOE, Office of Science, Basic Energy Sciences, Materials Sciences and Engineering Division. P. Bean at the University of Virginia is acknowledged for his SEM contributions measuring the HEASS. We acknowledge T. B. Gunnoe (University of Virginia), J. Elena (University of Virginia), D. E. Jiang (University of California, Riverside), and C. B. Murray (University of Pennsylvania) for the project discussion.

Author contributions: S.Z. and G.J. conceived and designed the experiments. W.A.G. and M.Y.Y. designed and performed the computational simulations. G.J. and C.L. performed the synthesis and analyzed experimental data with help from B.A. under the supervision of S.Z. and

S.D.. G.J. and D.A.D. collected and analyzed the SCXRD data. S.W., W.G., D.W. and S.B. performed STEM measurements of the materials. F.P. performed SSNMR experiments. G.J., and C.L. performed *operando* SAXS with assistance from H.Z. and X.Z.. F.M. and C.Z performed MALDI-TOF experiments. Z.X. and G.L. performed TGA experiments. G.J. measured the XPS and Raman spectra. G.J., M.Y.Y., W.A.G., and S.Z. wrote the manuscript. All authors discussed the results and commented on the manuscript.

Competing interests: Authors declare that they have no competing interests.

Figure Captions:

Figure 1. Schematic illustration of nanocluster superstructures formation process. Ceria and other rare earth oxide nanoclusters are assembled into superstructures through an OA-to-BA ligand-switching mechanism at high temperature. By further manipulating surface ligand chemistry, these structures may be disassembled into building blocks with OA and reassembled into superstructures at high temperature with BA. Building blocks may even be combined to form multi-element superstructures with the appropriate ligand treatments.

Figure 2. Superstructure morphology and *operando* SAXS monitoring superstructure formation. a-c, HAADF-STEM images of ceria superstructures show rod-like structures (**a**) generated from the self-assembly of 1.4 nm nanoclusters (**b, c**). **d**, *Operando* SAXS measurements performed at 1-minute intervals show a small shoulder at around q = 0.2 $Å^{-1}$ that is a result of the formation of nanoclusters in solution. This change occurs starting above 260 °C. **e**, Time evolution of the *operando* SAXS profile measured at 290 °C from t = 0 minutes when 290 °C is reached. Structure peaks associated with the *bct* superstructure appear at approximately 25 minutes and are indexed in the inset and in Supplementary Figure 3d at t = 60 minutes. **f**, ^{13}C {^{1}H} CPMAS

SSNMR of the washed and dried Ceria nanocluster in the pre-assembled, assembled, and disassembled forms. Disassembly was driven by introduction of OA in hexane. The resonances near 40 ppm are due to sp^3 hybridized C atoms while the resonance at 130 ppm indicates sp^2 hybridized C in aromatic moieties. **g**, Packing diagram generated from SCXRD of the disassembled Ceria nanoclusters recrystallized in pyridine and acetonitrile. Ce atoms are gold, oxygen atoms are red, and organic components are designated by wire frames.

Figure 3. MD simulations of nanocluster interactions. a, **b**, Model structures of OA-packed clusters (**a**) and BA-packed clusters (**b**). Each model contains 2 clusters (Ce: gold, O: red), 60 OAs (sky blue), 60 BAs (magenta), and 120 benzyl ethers (grey), where the BAs in the OA-packed model and the OAs in the BA-packed model were protonated. **c**, The distance between two clusters, where initial cluster-cluster distances were 2.1 nm (blue and red) and 3 nm (sky blue and orange). **d**, The average nonbonding energies (see the Coulombic and van der Waals components in **Supplementary Figures 12 a and b**, respectively) for 3 ns MD simulations (n = 3 runs). The energies are presented as the mean values +/- standard deviation (SD). Two models with different initial distances between nanoclusters were used for each system, 2.1 nm (blue and red) and 3 nm (sky blue and orange), respectively. pOA and pBA represent protonated OA and BA, respectively. **e,** Representative edge to face and (**f**) offset π-π interactions between intercluster BA ligands bound to adjacent CeO_x clusters from MD simulations.

Figure 4. Unit cell of the assemblies: size, benzyl ether, and structure. (**a**) The change in the cell volume as a function of the number of BAs from MD simulations. The dotted gray line indicates the cell volume of the experimental single-crystal structure. **b,** The cell volume as a function of the number of benzyl ethers incorporated into the superstructure, where the system contains 60 BAs (n = 3 runs). Each volume is presented +/- SD. **c,** Snapshot structure showing the

unit cell of the self-assembled structure, which is composed of 2 clusters, 60 BAs (purple), and 16 benzyl ethers (gray). **d,** $Ce_{24}O_{28}(OH)_8$ core nanocluster. BA ligands (not shown) contribute the remaining oxygens to the nanocluster. H atoms are omitted. Colour Code: Ce^{3+} - green, Ce^{4+} - gold, O^{2-} - red, OH – purple. **e,** BA coated nanoclusters, where dotted lines denote the unit cell. The poorly binding (111) facet opens a pocket for a close approach of the BA from a neighboring nanocluster, forcing alignment in the x direction.

Figure 5. Extended synthesis to other metal oxide superstructures. a-h, TEM images of LaO_x (**a**), SmO_x (**b**), YbO_x (**c**), HoO_x (**d**), EuO_x (**e**), ErO_x (**f**), TmO_x (**g**), and GdO_x (**h**) superstructures. **i,** *operando* SAXS measurement of LaO_x self-assembly. A rise at low q (< 0.05 $Å^{-1}$) and a structure peak at q = 0.407 $Å^{-1}$ are apparent at 110 minutes. The feature at q = 0.5 $Å^{-1}$ is an artefact of the measuring geometry and was present at all temperatures.

Figure 6. Multicomponent assemblies. a-d, TEM images of binary CeO_x/LaO_x (**a, b**) and CeO_x/SmO_x (**c, d**) superstructures. **e-g**, TEM images (**e,f**), HAADF-STEM image (**g**) and EDS elemental mapping (**h**, measured area is indicated in **g** using red frame) of the ternary $CeO_x/LaO_x/SmO_x$ superstructures (mapping colour code: Teal (Ce), Orange (Sm), and Yellow (La)).

References

1 Boles, M. A., Engel, M. & Talapin, D. V. Self-assembly of colloidal nanocrystals: from intricate structures to functional materials. *Chem. Rev.* **116**, 11220-11289, doi:10.1021/acs.chemrev.6b00196 (2016).

2 Li, Z., Fan, Q. & Yin, Y. Colloidal self-assembly approaches to smart nanostructured materials. *Chem. Rev.* **122**, 4976-5067, doi:10.1021/acs.chemrev.1c00482 (2021).

3 Urban, J. J., Talapin, D. V., Shevchenko, E. V., Kagan, C. R. & Murray, C. B. Synergism in binary nanocrystal superlattices leads to enhanced p-type conductivity in self-assembled PbTe/Ag_2Te thin films. *Nat. Mater.* **6**, 115-121, doi:10.1038/nmat1826 (2007).

4 Dong, A., Chen, J., Vora, P. M., Kikkawa, J. M. & Murray, C. B. Binary nanocrystal superlattice membranes self-assembled at the liquid-air interface. *Nature* **466**, 474-477, doi:10.1038/nature09188 (2010).

5 Koleilat, G. I. *et al.* Efficient, stable infrared photovoltaics based on solution-cast colloidal quantum dots. *ACS Nano* **2**, 833-840, doi:10.1021/nn800093v (2008).

6 Talapin, D. V., Lee, J. S., Kovalenko, M. V. & Shevchenko, E. V. Prospects of colloidal nanocrystals for electronic and optoelectronic applications. *Chem. Rev.* **110**, 389-458, doi:10.1021/cr900137k (2010).

7 Wang, P. *et al.* DNA origami guided self-assembly of plasmonic polymers with robust long-range plasmonic resonance. *Nano Lett.* **20**, 8926-8932, doi:10.1021/acs.nanolett.0c04055 (2020).

8 Ross, M. B., Ku, J. C., Vaccarezza, V. M., Schatz, G. C. & Mirkin, C. A. Nanoscale form dictates mesoscale function in plasmonic DNA-nanoparticle superlattices. *Nat. Nanotechnol.* **10**, 453-458, doi:10.1038/nnano.2015.68 (2015).

9 Lan, X. & Wang, Q. Self-assembly of chiral plasmonic nanostructures. *Adv. Mater.* **28**, 10499-10507, doi:10.1002/adma.201600697 (2016).

10 Kuzyk, A. *et al.* DNA-based self-assembly of chiral plasmonic nanostructures with tailored optical response. *Nature* **483**, 311-314, doi:10.1038/nature10889 (2012).

11 Shishou, K., Zhiyong, J., Nikles, D. E. & Harrell, J. W. Synthesis, self-assembly, and magnetic properties of $[FePt]_{1-x}Au_x$ nanoparticles. *IEEE Trans. Magn* **39**, 2753-2757, doi:10.1109/tmag.2003.815589 (2003).

12 Zeng, H., Li, J., Liu, J. P., Wang, Z. L. & Sun, S. Exchange-coupled nanocomposite magnets by nanoparticle self-assembly. *Nature* **420**, 395-398, doi:10.1038/nature01208 (2002).

13 Mohapatra, J. *et al.* Magnetic-field-induced self-assembly of FeCo/$CoFe_2O_4$ core/shell nanoparticles with tunable collective magnetic properties. *Nanoscale* **13**, 4519-4529, doi:10.1039/d1nr00136a (2021).

14 Chen, M., Kim, J., Liu, J. P., Fan, H. & Sun, S. Synthesis of FePt nanocubes and their oriented self-assembly. *J. Am. Chem. Soc.* **128**, 7132-7133, doi:10.1021/ja061704x (2006).

15 Liu, J. *et al.* Incorporation of clusters within inorganic materials through their addition during nucleation steps. *Nat. Commun.* **11**, 839-845, doi:10.1038/s41557-019-0303-0 (2019).

16 Kang, Y. *et al.* Design of Pt-Pd binary superlattices exploiting shape effects and synergistic effects for oxygen reduction reactions. *J. Am. Chem. Soc.* **135**, 42-45, doi:10.1021/ja3097527 (2013).

17 Kang, Y. *et al.* Engineering catalytic contacts and thermal stability: gold/iron oxide binary nanocrystal superlattices for CO oxidation. *J. Am. Chem. Soc.* **135**, 1499-1505, doi:10.1021/ja310427u (2013).

18 Baek, W. *et al.* Highly luminescent and catalytically active suprastructures of magic-sized semiconductor nanoclusters. *Nat. Mater.* **20**, 650-657, doi:10.1038/s41563-020-00880-6 (2021).

19 Li, S. *et al.* Single- and multi-component chiral supraparticles as modular enantioselective catalysts. *Nat. Commun.* **10**, 4826, doi:10.1038/s41467-019-12134-4 (2019).

20 Tang, Z., Zhang, Z., Wang, Y., Glotzer, S. C. & Kotov, N. A. Self-assembly of CdTe nanocrystals into free-floating sheets. *Science* **314**, 274-278, doi:10.1126/science.1128045 (2006).

21 Zhang, Z. & Glotzer, S. C. Self-assembly of patchy particles. *Nano Lett.* **4**, 1407-1413, doi:10.1021/nl0493500 (2004).

22 Liu, Q. *et al.* Self-assembly of polyoxometalate clusters into two-dimensional clusterphene structures featuring hexagonal pores. *Nat. Chem.* **14**, 433-440, doi: 10.1038/s41557-022-00889-1 (2022).

23 Nykypanchuk, D., Maye, M. M., van der Lelie, D. & Gang, O. DNA-guided crystallization of colloidal nanoparticles. *Nature* **451**, 549-552, doi:10.1038/nature06560 (2008).

24 Auyeung, E. *et al.* DNA-mediated nanoparticle crystallization into Wulff polyhedra. *Nature* **505**, 73-77, doi:10.1038/nature12739 (2014).

25 Yi, C. *et al.* Self-limiting directional nanoparticle bonding governed by reaction stoichiometry. *Science* **369**, 1369-1374, doi:10.1126/science.aba8653 (2020).

26 Young, K. L. *et al.* Assembly of reconfigurable one-dimensional colloidal superlattices due to a synergy of fundamental nanoscale forces. *Proc. Natl. Acad. Sci.* **109**, 2240-2245, doi:10.1073/pnas.1119301109 (2012).

27 Zeng, C., Chen, Y., Kirschbaum, K., Lambright, K. J. & Jin, R. Emergence of hierarchical structural complexities in nanoparticles and their assembly. *Science* **354**, 1580-1584, doi:10.1126/science.aak9750 (2016).

28 Nevers, D. R. *et al.* Mesophase formation stabilizes high-purity magic-sized clusters. *J. Am. Chem. Soc.* **140**, 3652-3662, doi:10.1021/jacs.7b12175 (2018).

29 Nagaoka, Y., Zhu, H., Eggert, D. & Chen, O. Single-component quasicrystalline nanocrystal superlattices through flexible polygon tiling rule. *Science* **362**, 1396-1400, doi:doi:10.1126/science.aav0790 (2018).

30 Smith, D. K., Goodfellow, B., Smilgies, D. M. & Korgel, B. A. Self-assembled simple hexagonal AB(2) binary nanocrystal superlattices: SEM, GISAXS, and defects. *J. Am. Chem. Soc.* **131**, 3281-3290, doi:10.1021/ja8085438 (2009).

31 Wu, L. *et al.* High-temperature crystallization of nanocrystals into three-dimensional superlattices. *Nature* **548**, 197-201, doi:10.1038/nature23308 (2017).

32 Sun, Y. *et al.* Quantitative 3D evolution of colloidal nanoparticle oxidation in solution. *Science* **356**, 303-307, doi:10.1126/science.aaf6792 (2017).

33 Qiao, L. *et al.* Standardizing size- and shape-controlled synthesis of monodisperse magnetite (Fe_3O_4) nanocrystals by identifying and exploiting effects of organic impurities. *ACS Nano* **11**, 6370-6381, doi:10.1021/acsnano.7b02752 (2017).

34 Pinna, N., Garnweitner, G., Beato, P., Niederberger, M. & Antonietti, M. Synthesis of yttria-based crystalline and lamellar nanostructures and their formation mechanism. *Small* **1**, 112-121, doi:10.1002/smll.200400014 (2005).

35 Haffad, D., Kameswari, U., Bettahar, M. M., Chambellan, A. & Lavalley, J. C. Reduction of benzaldehyde on metal oxides. *J. Catal.* **172**, 85-92, doi:DOI 10.1006/jcat.1997.1854 (1997).

36 Pell, A. J. & Pintacuda, G. Broadband solid-state MAS NMR of paramagnetic systems. *Prog. Nucl. Magn. Reson. Spectrosc.* **84-85**, 33-72, doi:10.1016/j.pnmrs.2014.12.002 (2015).

37 Badr, Y. & Mahmoud, M. A. Size-dependent surface-enhanced Raman scattering of sodium benzoate on silver nanoparticles. *J. Mol. Struct.* **749**, 187-192, doi:10.1016/j.molstruc.2005.04.012 (2005).

38 Mitchell, K. J., Abboud, K. A. & Christou, G. Atomically-precise colloidal nanoparticles of cerium dioxide. *Nat. Commun.* **8**, 1445, doi:10.1038/s41467-017-01672-4 (2017).

39 Mitchell, K. J. et al. Expansion of the Family of Molecular Nanoparticles of Cerium Dioxide and Their Catalytic Scavenging of Hydroxyl Radicals. Inorg Chem 60, 1641-1653 (2021). https://doi.org:10.1021/acs.inorgchem.0c03133

40 Cargnello, M. *et al.* Substitutional doping in nanocrystal superlattices. *Nature* **524**, 450-453, doi:10.1038/nature14872 (2015).

41 Xie, P. *et al.* Highly efficient decomposition of ammonia using high-entropy alloy catalysts. *Nat. Commun.* **10**, doi:10.1038/s41467-019-11848-9 (2019).

42 Yao, Y. *et al.* Carbothermal shock synthesis of high-entropy-alloy nanoparticles. *Science* **359**, 1489-1494, doi:doi:10.1126/science.aan5412 (2018).
43 Sheldrick, G. M. SHELXT - integrated space-group and crystal-structure determination. *Acta Crystallogr. A: Found. Adv.* **71**, 3-8, doi:10.1107/S2053273314026370 (2015).
44 Dolomanov, O. V., Bourhis, L. J., Gildea, R. J., Howard, J. A. K. & Puschmann, H. OLEX2: a complete structure solution, refinement and analysis program. *J. Appl. Crystallogr.* **42**, 339-341, doi:10.1107/S0021889808042726 (2009).
45 Rappe, A. K., Casewit, C. J., Colwell, K. S., Goddard, W. A. & Skiff, W. M. UFF, a full periodic-table force-field for molecular mechanics and molecular-dynamics simulations. *J. Am. Chem. Soc.* **114**, 10024-10035, doi:DOI 10.1021/ja00051a040 (1992).
46 Jo, S., Kim, T., Iyer, V. G. & Im, W. CHARMM-GUI: a web-based graphical user interface for CHARMM. *J. Comput. Chem.* **29**, 1859-1865, doi:10.1002/jcc.20945 (2008).
47 Shirts, M. R. *et al.* Lessons learned from comparing molecular dynamics engines on the SAMPL5 dataset. *J. Comput. Aided Mol. Des.* **31**, 147-161 (2017).
48 Plimpton, S. Fast parallel algorithms for short-range molecular-dynamics. *J. Comput. Phys.* **117**, 1-19, doi:DOI 10.1006/jcph.1995.1039 (1995).
49 Martinez, L., Andrade, R., Birgin, E. G. & Martinez, J. M. PACKMOL: a package for building initial configurations for molecular dynamics simulations. *J. Comput. Chem.* **30**, 2157-2164, doi:10.1002/jcc.21224 (2009).
50 Humphrey, W., Dalke, A. & Schulten, K. VMD: visual molecular dynamics. *J. Mol. Graph.* **14**, 33-38, 27-38, doi:10.1016/0263-7855(96)00018-5 (1996).

Table of Contents

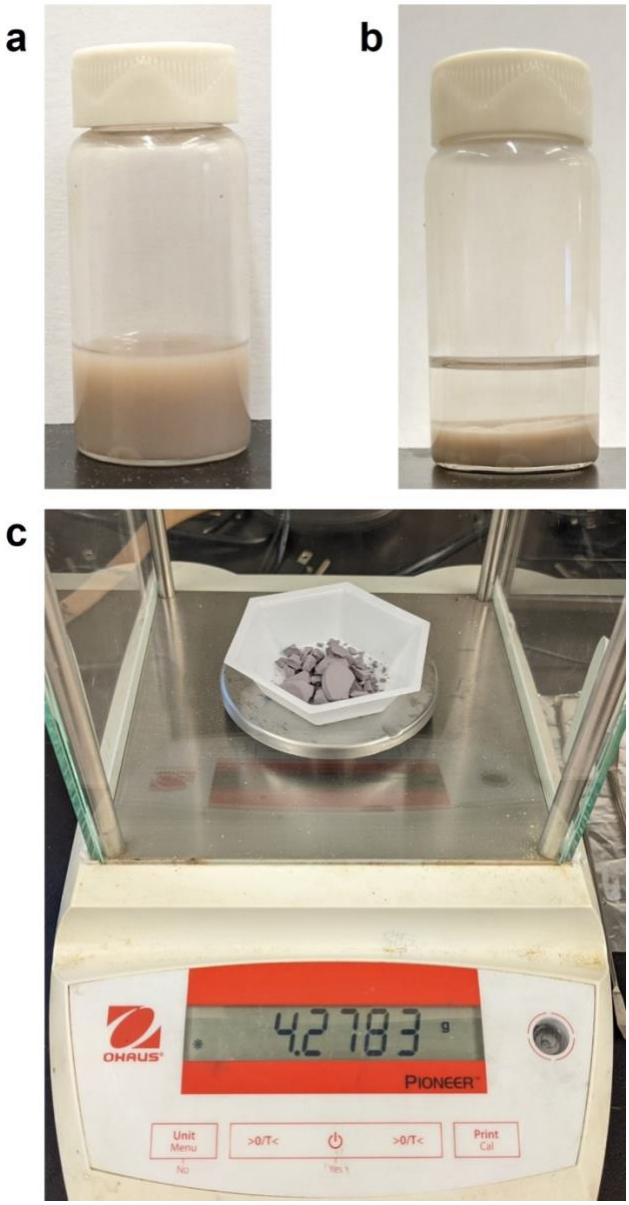

Supplementary Figure 1. Images of the Ceria superstructures. (**a**) dispersed in hexanes, (**b**) settled out of hexanes, and (**c**) dried to a powder. The powder dried sample was weighed to demonstrate the scalability of this synthesis.

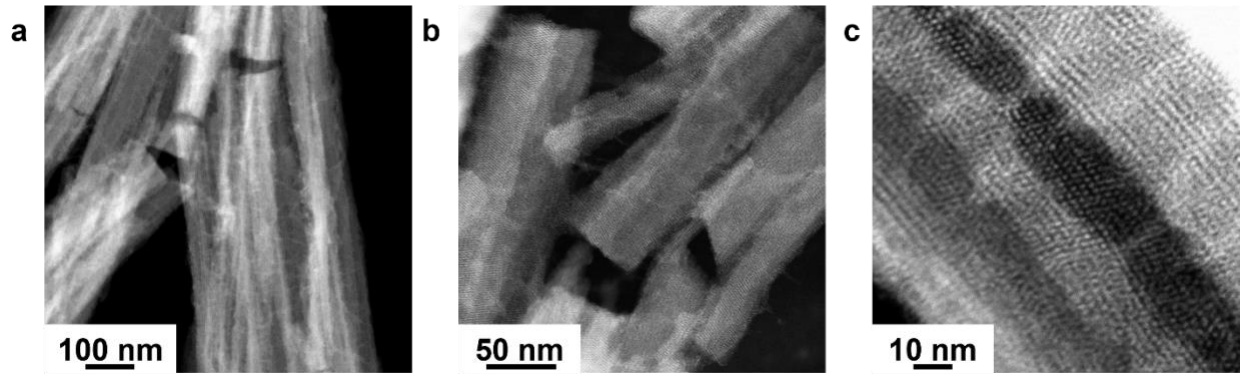

Supplementary Figure 2. HAADF-STEM images of Ceria superstructures. HAADF-STEM images of ceria nanocluster assemblies at different magnifications.

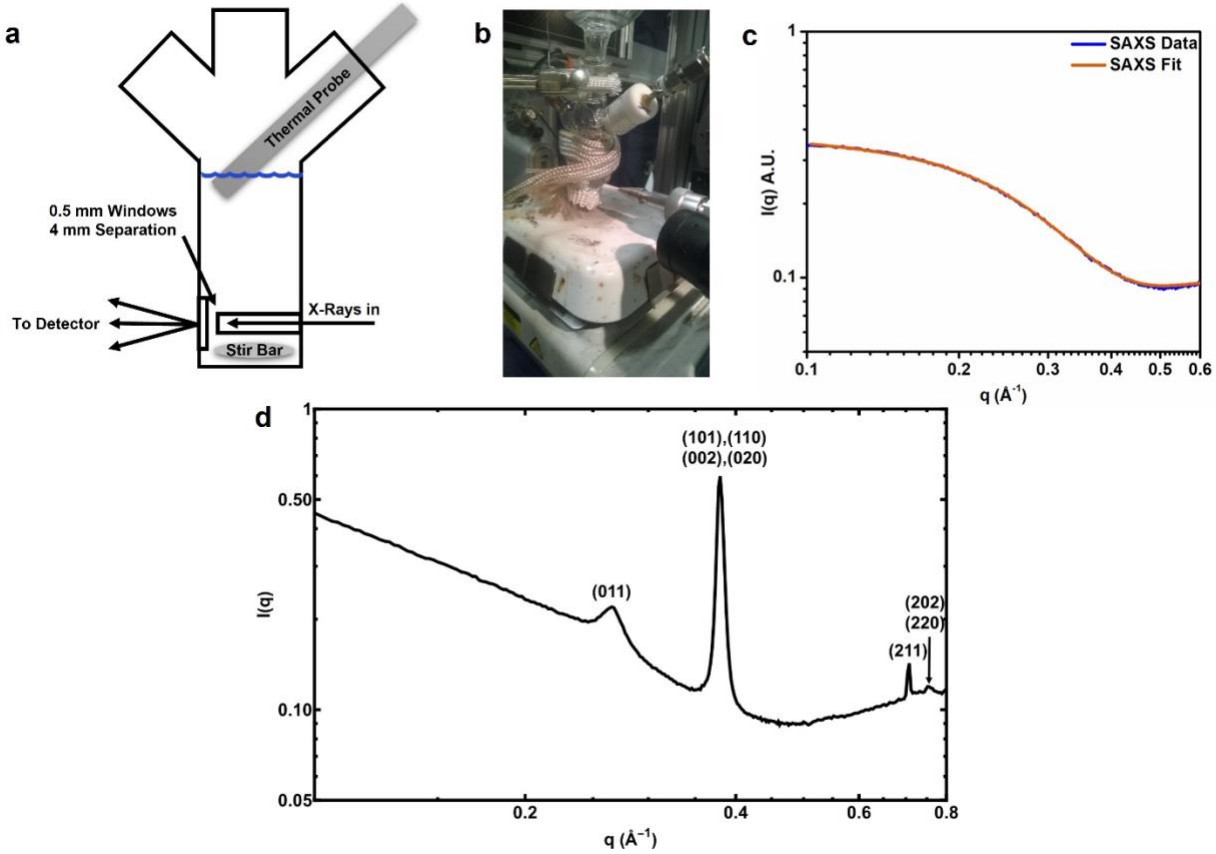

Supplementary Figure 3. *Operando* SAXS. Schematic illustration of the *operando* SAXS reactor (**a**) and picture of reactor setup (**b**) at 12-ID-B beamline at the Advanced Photon Source of Argonne National Lab. The reactor holds up to 15 mL of reactant. Heating tape is wrapped around the reactor with space left open for the X-ray beam. The beam passes through two 0.5 mm windows with 4 mm between them for sample. A condenser is affixed to the top of the reactor and a rubber septum is used to seal the reactor from the atmosphere. (**c**) A hard sphere model fit of the T = 290 °C SAXS profile in Fig. 2d indicates particles with radii of around 0.89 nm have been formed. (**d**) SAXS profile at t = 60 min during *operando* SAXS measurement for monitoring Ceria superstructure formation.

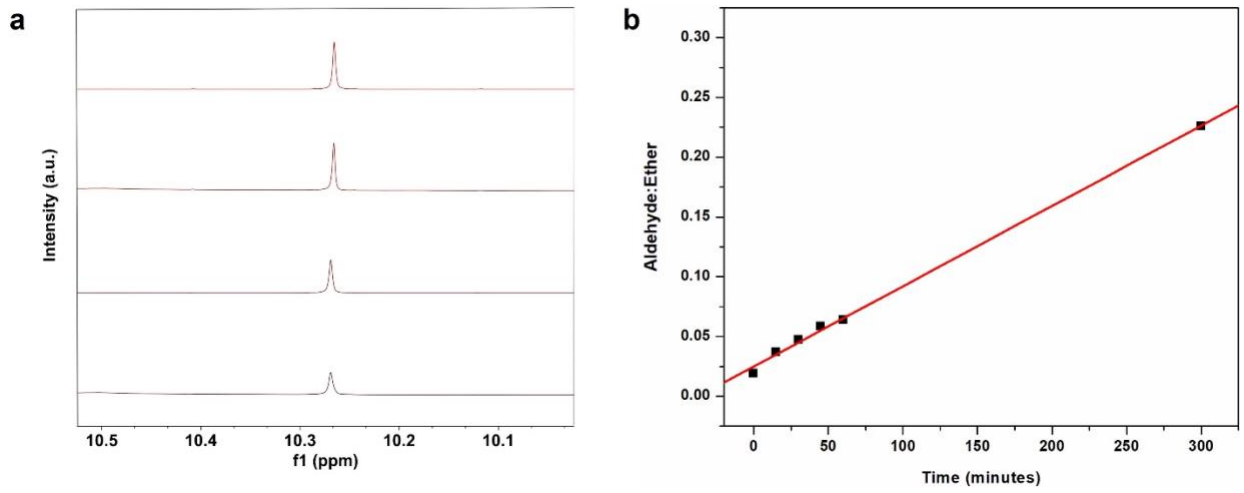

Supplementary Figure 4. ^{1}H NMR spectra of solvent. (a) Benzaldehyde ^{1}H NMR signal increases over time while the benzyl ether is heated at 290 °C. (**b**) Ratio of the benzaldehyde aldehyde proton to the methylene protons of benzyl ether as measured in ^{1}H NMR shows an increase of aldehyde as the solvent is held under reaction conditions without Ce precursor at 290 °C.

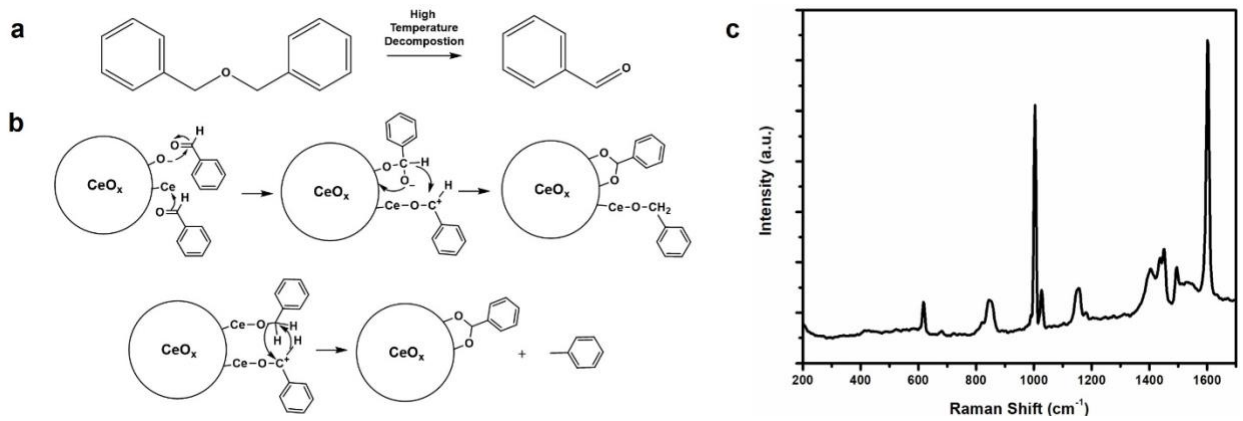

Supplementary Figure 5. BA formation mechanism and Raman spectrum. Proposed mechanism to generate BA from benzyl ether. (**a**) At high temperature, a small amount of benzyl ether decomposes to form benzaldehyde as shown in Supplementary Figure 4. (**b**) This may react through a Cannizzaro type mechanism catalyzed by the metal oxide. The benzyl alcohol formed by this mechanism reacts with benzaldehyde to generate more BA ligands and toluene, which evaporates off. (**c**) Raman spectrum demonstrating chemical signatures of BA moieties on the ceria superstructure sample.

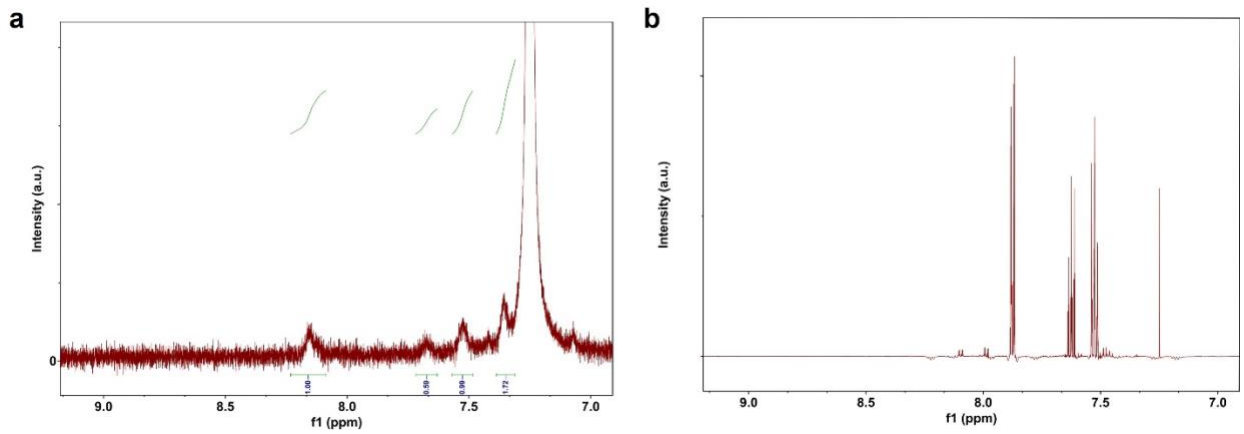

Supplementary Figure 6. ^{1}H NMR spectra of superstructures. (**a**) ^{1}H NMR spectrum of solvated superstructures in $CDCl_3$ (7.25 ppm) in the region typical of aryl protons. Resonances at 7.52 ppm, 7.68 ppm, and 8.15 ppm are present in a 2:1:2 ratio and correspond to BA. The resonance at 7.36 ppm corresponds with benzyl ether solvent. The absence of a peak at 7.88 ppm (and 10.26 ppm) indicates that benzaldehyde is not present in a significant amount in this sample. (**b**) ^{1}H NMR spectrum in the same region of benzaldehyde in $CDCl_3$. Major resonances are centered around 7.53 ppm, 7.62 ppm, and 7.88 ppm.

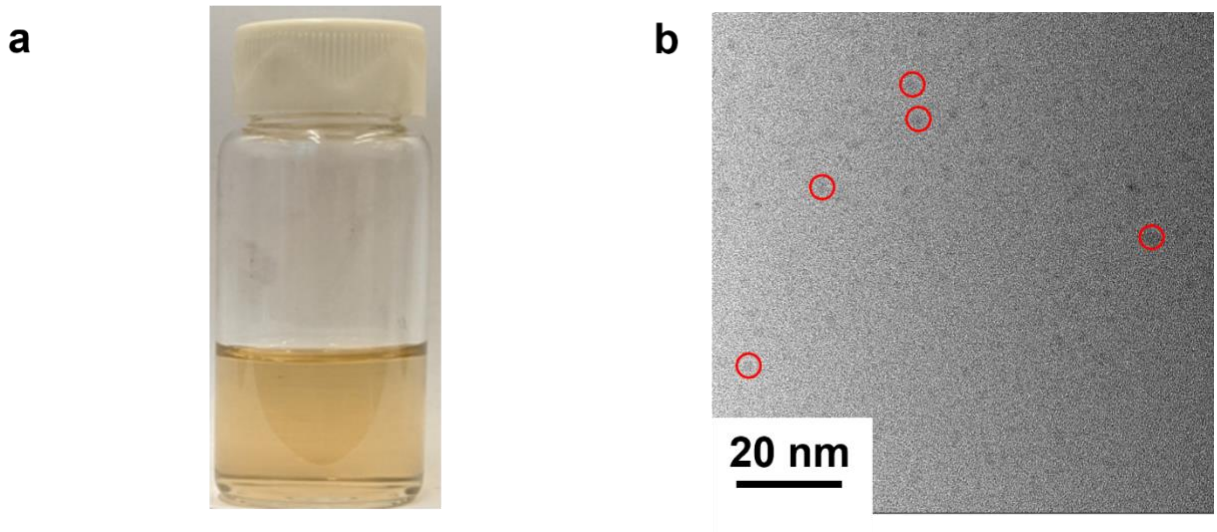

Supplementary Figure 7. Oleic acid dispersed nanoclusters. (**a**) Golden brown dispersion of Ceria nanoclusters disassembled from superstructure in hexane by adding oleic acid. (**b**) TEM image of Ceria superstructure treated with oleic acid. The small particles have low contrast with the background and are circled in red to guide the eye.

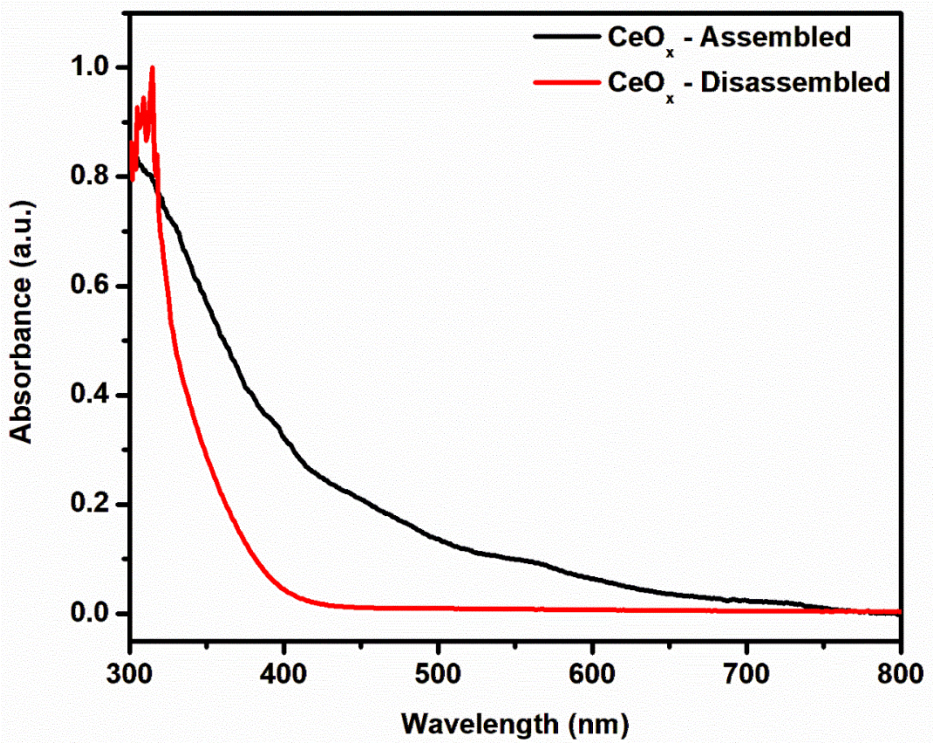

Supplementary Figure 8. UV-Vis spectra of assembled and disassembled Ceria. UV-Vis spectra of ceria assemblies and disassembled particles.

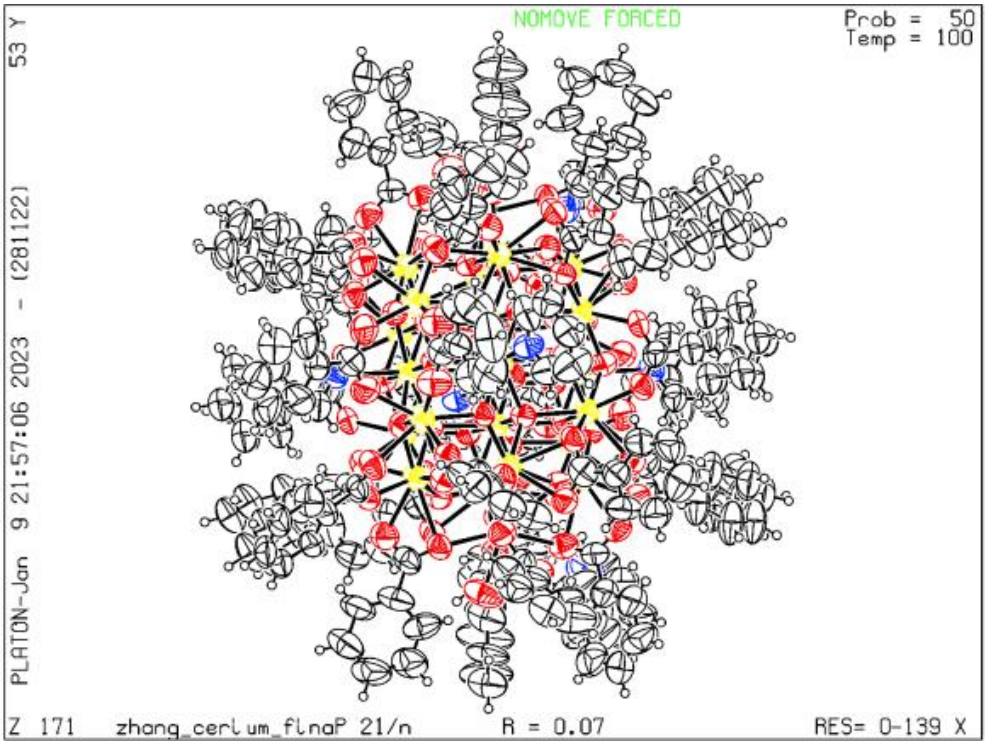

Supplementary Figure 9. Ceria nanocluster crystal structure with thermal ellipsoids. Nanocluster structure as observed in SCXRD. C atoms are in black, O atoms are red, N atoms are blue, and Ce atoms are yellow. Thermal ellipsoids are set at 50% probability level. CCDC reference number: 2157579.

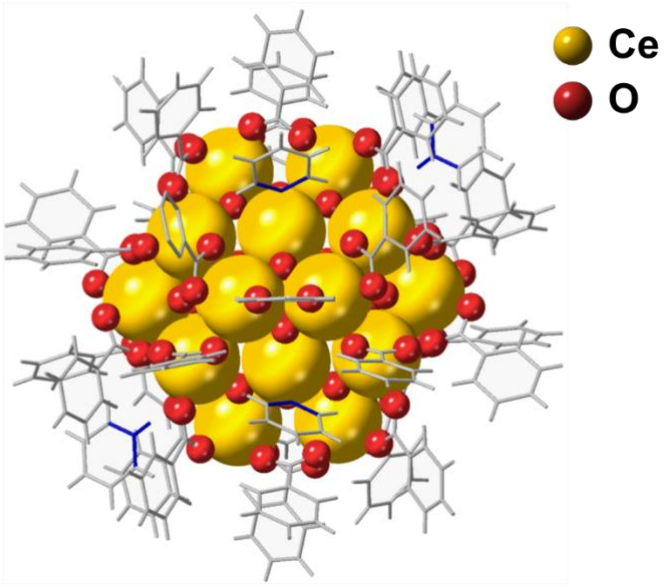

Supplementary Figure 10. Ceria nanocluster structure with pyridine. Full model of the $Ce_{24}O_{28}(OH)_8$ nanocluster ligated by 30 BAs and 8 pyridines. 4 pyridines directly bind Ce at the (111) facet and 4 interact through H-bonding. Ce atoms are in gold, oxygen atoms are red, BA and pyridine ligands are shown in wire format with N atom bonds of the pyridine highlighted in blue.

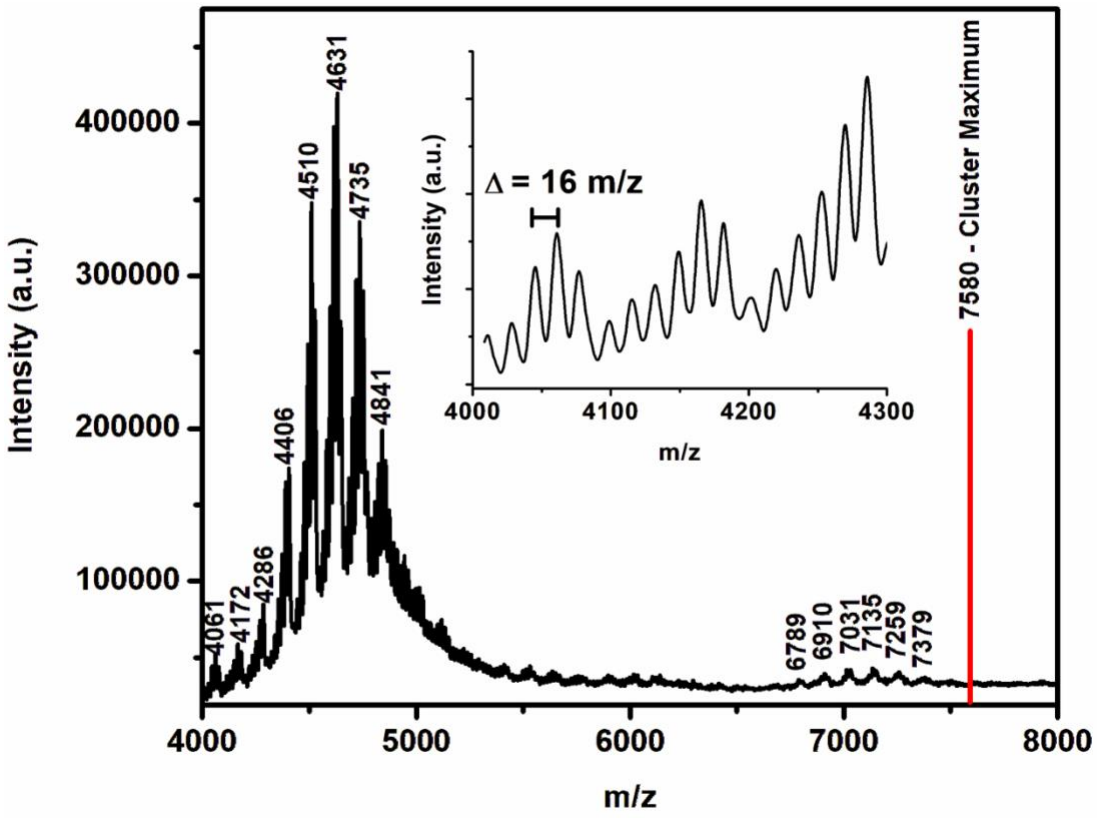

Supplementary Figure 11. MALDI-TOF analysis of DMF disassembled Ceria. MALDI-TOF spectrum of DMF disassembled Ceria. The first peak observed in this spectrum is 120 amu above $Ce_{24}O_{28}(OH)_8$ and corresponds to a singly deprotonated cluster with a BA ligand. The inset shows how the peaks are subdivided further by 16 amu units. This is assigned to changes in the oxygen numbers of the cluster and may originate either from O loss or dissociation of the BA ligand. The peaks terminate prior to the $Ce_{24}O_{28}(OH)_8(BA)_{30}$ maximum of 7580 amu.

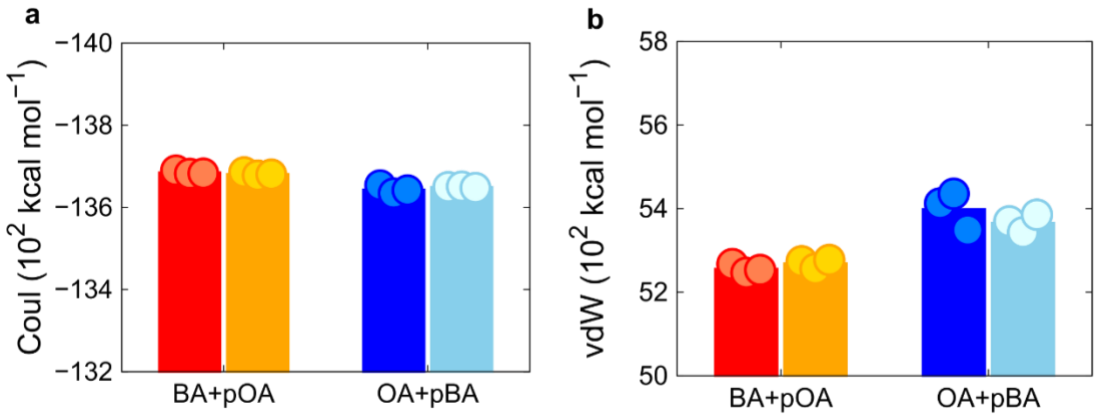

Supplementary Figure 12. Contributions of non-bonding energies. Components of the non-bonding coulombic (**a**) and van der Waals (**b**) energies described in **Fig. 3d.** for a 3 ns MD simulation (n = 3 runs). Each energy is presented as the mean +/- standard deviation (SD). Two models with different initial inter-cluster distances were used for each system: 2.1 nm (blue and red) and 3 nm (sky blue and orange). pOA and pBA represent protonated OA and BA, respectively.

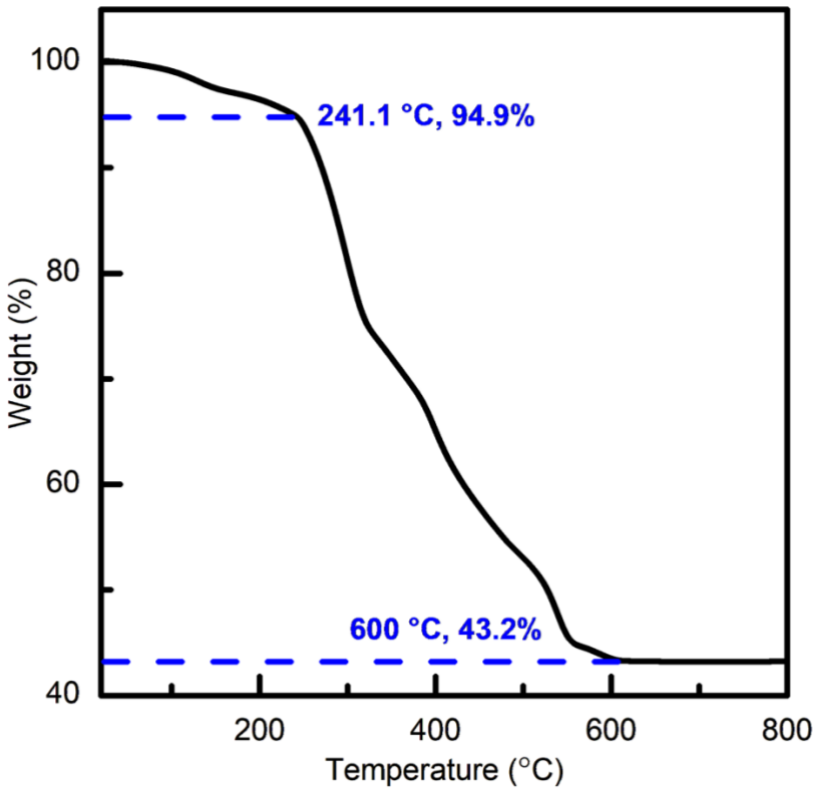

Supplementary Figure 13. TGA result of Ceria superstructures. The final product is assumed to be $Ce_{24}O_{48}$ with a mass of 4154.4 amu due to the treatment in high temperature/ high O_2 conditions. The initial 5.1% weight reduction is assigned to residual solvent on the sample and is neglected for final mass calculations.

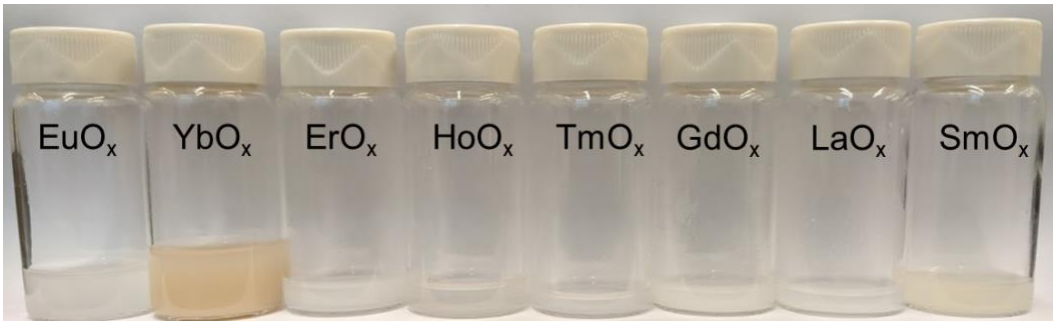

Supplementary Figure 14. Images of other rare earth oxide superstructures. Sample images of EuO_x, YbO_x, ErO_x, HoO_x, TmO_x, GdO_x, LaO_x, and SmO_x.

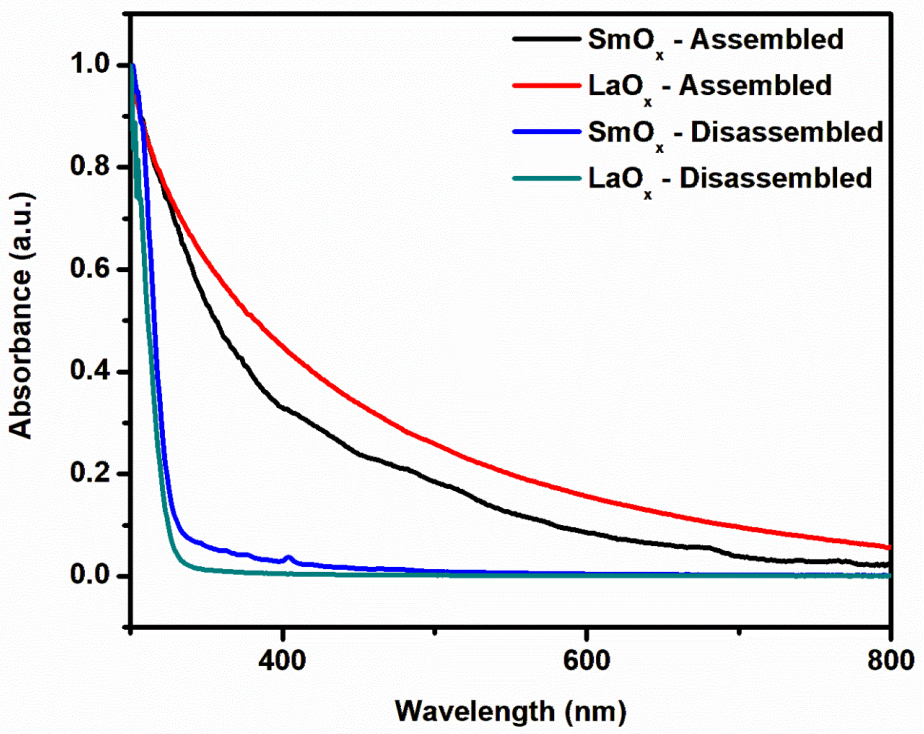

Supplementary Figure 15. UV-Vis spectra of other rare earth oxides. UV-Vis spectra of SmO_x and LaO_x in both assembled and disassembled states.

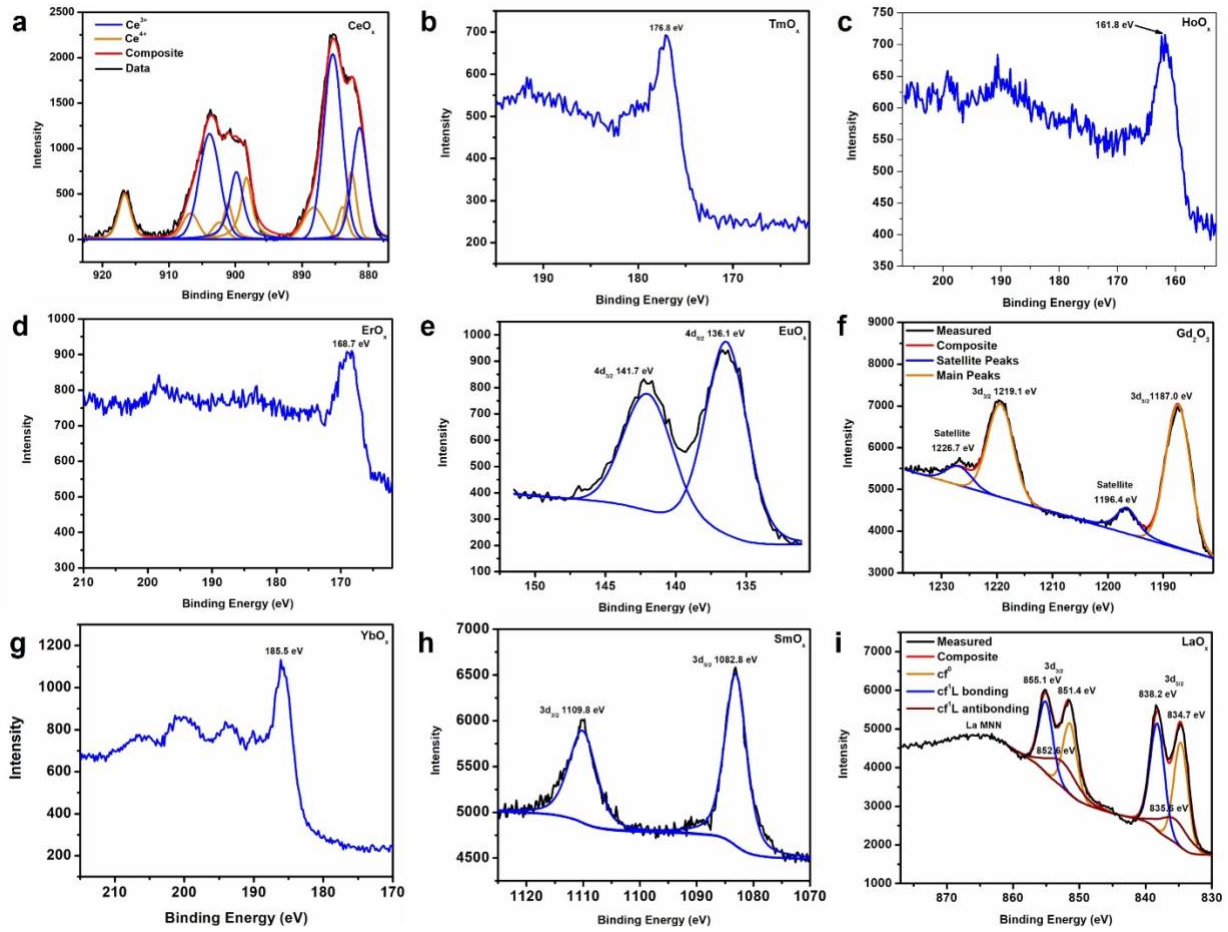

Supplementary Figure 16. XPS results of rare earth oxide superstructures. (**a**) Background subtracted Ce 3d XPS spectrum of Ceria superstructure. Deconvolution of the peaks was performed according to Skala *et al.*[1] This suggests around 80% Ce^{4+} content. (**b**) XPS spectrum of the Tm 4d region. The peak at 176.8 eV agrees with Tm^{3+} in Tm_2O_3 as reported by Aguilar *et al.*[2] (**c**) XPS spectrum of the Ho 4d region. The peak at 161.8 eV agrees with Ho^{3+} of Ho_2O_3 reported by Pan *et al.*[3] (**d**) XPS spectrum of the Er 4d region. The peak at 168.7 eV agrees with the previously reported Er_2O_3 value of 168.9 eV.[4] (**e**) XPS spectrum of the Eu 4d region shows the $4d_{5/2}$ peak at 136.1 eV, which is slightly higher than the reported Eu_2O_3 value but agrees with Eu^{3+} in $Eu(acac)_3$.[5] This could be a result of the high surface area to volume ratio ligated by carboxylates. (**f**) XPS spectrum of the Gd 3d region. The signals at 1187.0 eV, 1219.1 eV, and the satellite at 1196.4 eV agree with previous results of Gd_2O_3.[6] (**g**) XPS spectrum of the Yb 4d region. The measured value at 185.5 eV and profile agrees with Yb^{3+} in Yb_2O_3.[7] (**h**) XPS spectrum of the Sm 3d region. The measured values at 1082.8 eV and 1109.8 eV agree with reported values for Sm_2O_3.[8] (**i**) XPS spectrum of the La 3d region and the overlapping La MNN Auger region. The results agree with a La^{3+} with a value of $3d_{5/2}$ doublet at 834.8eV and 838.3 eV along with a $3d_{3/2}$ doublet at 851.6 eV and 855.1 eV.[9] The split on these doublets, from charge transfer with the O, is 3.5 eV and is smaller than is typically seen with La_2O_3, but is more typical of $La_2(CO_3)_3$. This could be a result of the high surface area ligated by carboxylate type species.

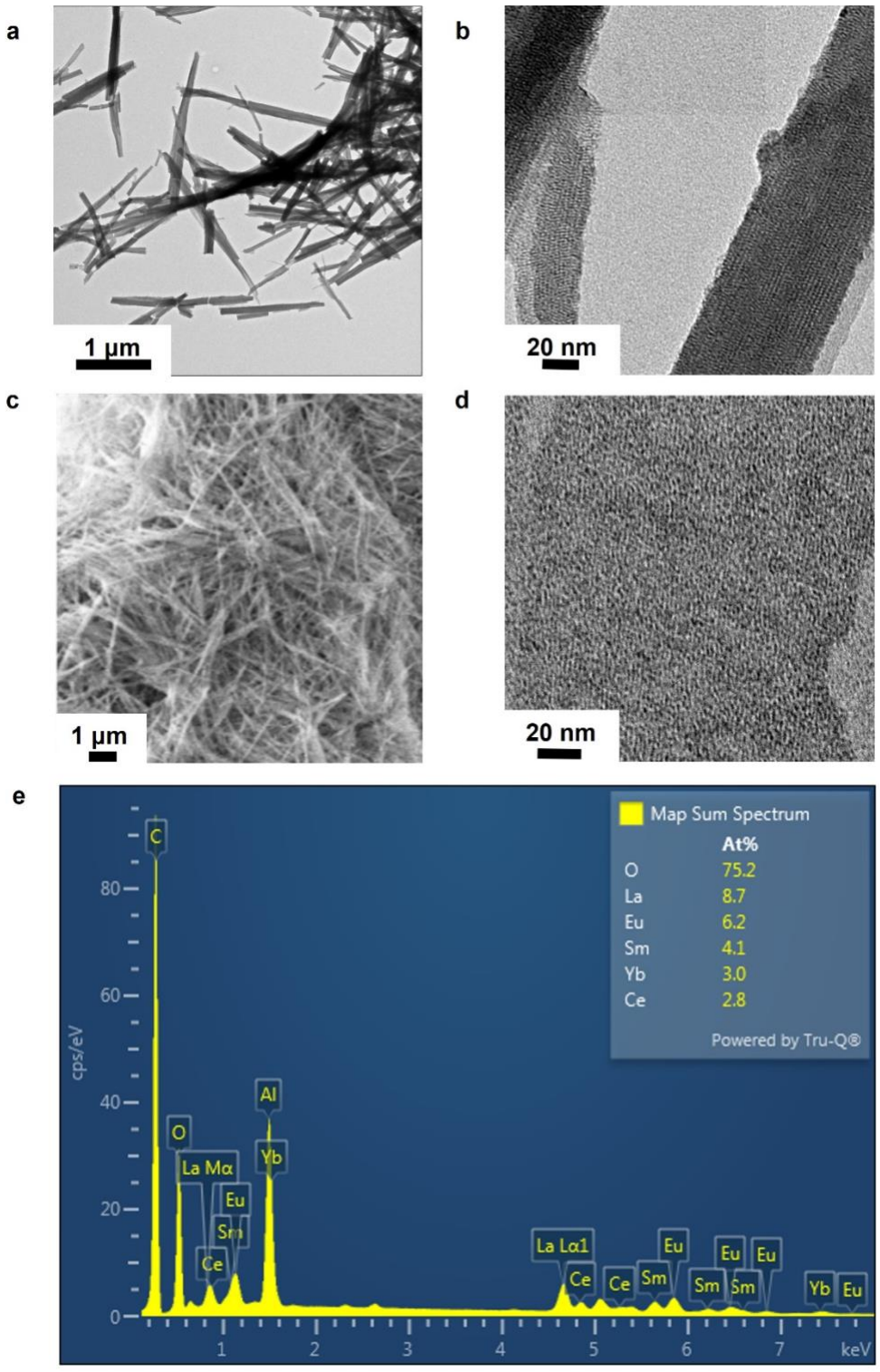

Supplementary Figure 17. HEAAS. TEM images of the (**a**) macrostructure and (**b**) microstructure of Ceria superstructures re-assembled from oleic acid disassembled superstructures. (**c**) SEM image of the penta-component HEAAS. (**d**) TEM image showing the assembled structure of the penta-component superstructure. (**e**) EDS spectrum showing the presence of 5 elements (La, Eu, Sm, Yb, and Ce) used to prepare the superstructures.

Supplementary Table 1: Raman peak comparison. A peak-by-peak comparison of the measured Raman peaks with those reported of sodium benzoate[10].

Assignment[10]	CeOx Superstructure (cm^{-1})	Published (cm^{-1})
ν(C=O)	1602	1603
ν(C*C)	-	1575
ν(C-C)	1494	1492
ν(C-C)	1435	1438
$\nu(COO^-)$	1403	1400
ν(C-O)	-	1290
β(C-H)	1180	1184
β(C-H)	1157	1159
β(C-H)	1146	1142
β(C-H)	1027	1030
Ring Breathing	1004	1004
$\nu(C\text{-}COO^-)$	846	843
γ(C-H)	820	820
Ring Breathing	680	679
β(OCO)	619	615
Ring of Out of Plane Skeletal Vibration	414	401

Supplementary References

1 Skála, T., Šutara, F., Prince, K. C. & Matolín, V. Cerium oxide stoichiometry alteration via Sn deposition: influence of temperature. *J. Electron Spectrosc. Relat. Phenom.* **169**, 20-25, doi:10.1016/j.elspec.2008.10.003 (2009).

2 Aguilar, T. *et al.* Surface thulium-doped TiO_2 nanoparticles used as photoelectrodes in dye-sensitized solar cells: improving the open-circuit voltage. *Appl. Phys.* **121**, 1261-1269, doi:10.1007/s00339-015-9503-7 (2015).

3 Pan, T.-M., Chang, W.-T. & Chiu, F.-C. Structural and electrical properties of thin Ho_2O_3 gate dielectrics. *Thin Solid Films* **519**, 923-927, doi:https://doi.org/10.1016/j.tsf.2010.09.002 (2010).

4 Armelao, L. *et al.* Silica-supported erbium-based nanosystems: an XPS characterization. *Surf. Sci. Spectra* **11**, 26-32, doi:10.1116/11.20050102 (2004).

5 Mercier, F., Alliot, C., Bion, L., Thromat, N. & Toulhoat, P. XPS study of Eu(III) coordination compounds: Core levels binding energies in solid mixed-oxo-compounds $Eu_mX_xO_y$. *J. Electron Spectrosc. Relat. Phenom.* **150**, 21-26, doi:10.1016/j.elspec.2005.08.003 (2006).

6 Milanov, A. P. *et al.* Lanthanide oxide thin films by metalorganic chemical vapor deposition employing volatile guanidinate precursors. *Chem. Mater.* **21**, 5443-5455, doi:10.1021/cm902123m (2009).

7 Hagström, S. B. M., Hedén, P. O. & Löfgren, H. Electron density of states in Yb metal as observed by X-ray photoemission. *Solid State Comm.* **8**, 1245-1248, doi:10.1016/0038-1098(70)90369-8 (1970).

8 Myhre, K., Burns, J., Meyer, H., Sims, N. & Boll, R. Samarium electrodeposited acetate and oxide thin films on stainless steel substrate characterized by XPS. *Surf. Sci. Spectra* **23**, 70-81, doi:10.1116/1.4954390 (2016).

9 Li, J. P. H. *et al.* Understanding of binding energy calibration in XPS of lanthanum oxide by in situ treatment. *Phys. Chem. Chem. Phys.* **21**, 22351-22358, doi:10.1039/c9cp04187g (2019).

10 Badr, Y. & Mahmoud, M. A. Size-dependent surface-enhanced Raman scattering of sodium benzoate on silver nanoparticles. *J. Mol. Struct.* 749, 187-192, doi:10.1016/j.molstruc.2005.04.012 (2005).